Probing the Dynamics of a Nuclear Spin Bath in Diamond through Time-Resolved Central Spin Magnetometry

A. Dréau,[1,*] P. Jamonneau,[1] O. Gazzano,[2] S. Kosen,[1] J.-F. Roch,[1] J. R. Maze,[3] and V. Jacques[1,†]
[1]Laboratoire Aimé Cotton, CNRS, Université Paris-Sud and Ecole Normale Supérieure de Cachan, 91405 Orsay, France
[2]Universität des Saarlandes, Fachrichtung 7.2 (Experimentalphysik), Campus E2.6, 66123 Saarbrücken, Germany
[3]Facultad de Física, Pontificia Universidad Católica de Chile, Santiago 7820436, Chile
(Received 19 June 2014; published 22 September 2014)

Using fast electron spin resonance spectroscopy of a single nitrogen-vacancy defect in diamond, we demonstrate real-time readout of the Overhauser field produced by its nuclear spin environment under ambient conditions. These measurements enable narrowing the Overhauser field distribution by postselection, corresponding to a conditional preparation of the nuclear spin bath. Correlations of the Overhauser field fluctuations are quantitatively inferred by analyzing the Allan deviation over consecutive measurements. This method allows us to extract the dynamics of weakly coupled nuclear spins of the reservoir.

DOI: 10.1103/PhysRevLett.113.137601 PACS numbers: 76.30.Mi, 03.65.Yz, 42.50.Lc, 71.70.Jp

Spins in solids are textbook platforms to model and investigate the dynamics of open quantum systems. A ubiquitous example consists of a central electronic spin, described as a two-level system, interacting through hyperfine coupling with a mesoscopic bath of nuclear spins. This interaction is identified as the major source of decoherence for solid-state spin qubits [1–3]. Measuring and controlling the dynamics of such complex environments is, therefore, a central challenge in quantum physics [4–7], with potential applications in solid-state quantum information processing [8] and metrology [9–11].

In this Letter, we explore the dynamics of a dilute nuclear spin bath interacting with the electronic spin of a single nitrogen-vacancy (NV) color center in diamond. This atomic-sized defect has attracted considerable interest over the last years because its ground state is an electronic spin triplet $S = 1$ that can be optically initialized, coherently manipulated with microwave magnetic fields and readout by optical means [12]. In ultrapure diamond samples, decoherence of the NV center electronic spin is mainly caused by interaction with a bath of ^{13}C nuclear spins ($I_c = 1/2$) randomly dispersed in the diamond lattice [3,13–15]. As shown in Fig. 1, each ^{13}C nuclear spin n of the bath induces a hyperfine splitting $\mathcal{A}^{(n)}$ of the NV spin sublevels, whose amplitude depends on its lattice site position with respect to the NV defect [16–19]. All hyperfine splittings from the nuclear spin bath add up, resulting in a quasicontinuum distribution of hyperfine lines. Each nuclear spin configuration of the bath produces an effective hyperfine magnetic field, colloquially known as an "Overhauser field," which randomly fluctuates through nuclear spin flips. In most experiments, these fluctuations are much faster than the measurement time scale, so that statistical averaging over all the configurations of the ^{13}C nuclear spin environment leads to an inhomogeneous linewidth Γ_2^* of the NV defect electron spin resonance (ESR) [14,15], as shown in the right panel of Fig. 1. This limitation can be circumvented by performing measurements faster than the correlation time of the nuclear spin bath. This can be achieved at cryogenic temperatures by using Overhauser field-selective dark resonances in a Λ-type level configuration [7]. Here, we follow an alternative approach which simply consists of acquisitions of optically detected ESR spectra under ambient conditions. The NV defect is used as a magnetometer to infer the instantaneous Overhauser field and its dynamics through the detection of Zeeman shifts of the ESR frequency induced by nuclear spin flips in the local environment.

A central idea of this Letter is to apply a static magnetic field B along the NV defect axis (z) in order to tune the correlation time of the nuclear spin environment. Indeed,

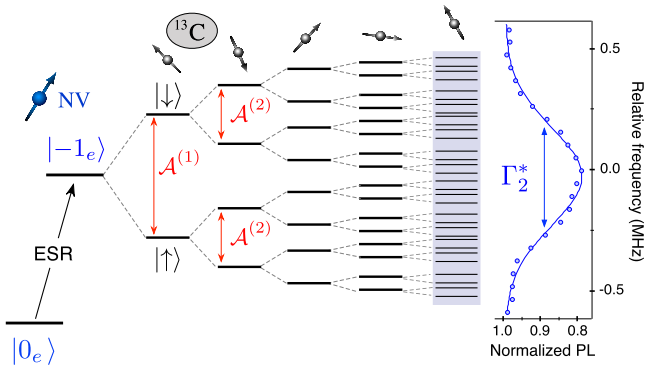

FIG. 1 (color online). Hyperfine structure of a single NV defect interacting with nearby ^{13}C nuclear spins. Hyperfine sublevels linked to the intrinsic ^{14}N nuclear spin of the NV defect are not shown. The right panel shows a typical spectrum of the ESR transition between the $m_s = 0$ [$|0_e\rangle$] and $m_s = -1$ [$|-1_e\rangle$] electron spin sublevels.

the flipping rate $\gamma_R^{(n)}$ of each ^{13}C nuclear spin of the bath weakly coupled by hyperfine interaction with the NV defect electronic spin can be written as [20]

$$\gamma_R^{(n)} = \frac{1}{T_R^{(n)}} \propto \frac{[\mathcal{A}_{\mathrm{ani}}^{(n)}]^2}{[\mathcal{A}_{\mathrm{ani}}^{(n)}]^2 + (\mathcal{A}_{\mathrm{zz}}^{(n)} - \gamma_n B)^2}, \quad (1)$$

where $\mathcal{A}_{\mathrm{ani}}^{(n)}$ and $\mathcal{A}_{\mathrm{zz}}^{(n)}$ are the anisotropic and longitudinal (zz) components of the hyperfine tensor, which depend on the lattice site position of the ^{13}C with respect to the NV defect, and $\gamma_n \approx 1.07$ kHz/G is the ^{13}C gyromagnetic ratio. The nuclear spin lifetime $T_R^{(n)}$ evolves quadratically with the magnetic field and can reach few seconds at high fields ($B > 2000$ G) for ^{13}C with hyperfine coupling strengths $\mathcal{A}^{(n)}$ weaker than 200 kHz [20–22]. This is long enough to be detected through fast ESR spectroscopy under ambient conditions.

Individual NV defects in a high-purity diamond sample with a natural abundance of ^{13}C (1.1%) are optically addressed at room temperature using a scanning confocal microscope. In such samples, the inhomogeneous ESR linewidth Γ_2^* is a few hundred kHz (Fig. 1) [13–15]. A permanent magnet placed on a three-axis translation stage is used to apply a static magnetic field along the NV defect axis (z). Spectroscopy of the ESR transition between the $m_s = 0$ and $m_s = -1$ electron spin sublevels is performed through repetitive excitation of the NV defect with a resonant microwave (MW) π pulse followed by a 300-ns readout laser pulse [23]. This sequence is continuously repeated during 30 ms while recording the spin-dependent photoluminescence (PL) intensity of the NV defect, before incrementing the MW frequency. All ESR spectra shown in this work were recorded on 15 points, corresponding to a measurement time $T_m \sim 450$ ms per spectrum. In practice, three MW sources are swept simultaneously in order to optimize the ESR contrast and to get rid of the dynamics linked to the intrinsic ^{14}N nuclear spin ($I_N = 1$) of the NV defect [24]. The MW sources are synchronized and their frequencies detuned by $\mathcal{A}_N = 2.16$ MHz, which corresponds to the hyperfine splitting induced by the ^{14}N nucleus (see the Supplemental Material [25]).

Intensity plots of consecutive ESR spectra recorded from a single NV defect are depicted in Fig. 2(a) for three different magnetic field amplitudes. For each individual spectrum i, the instantaneous ESR frequency $f(i)$ was extracted through data fitting with a Gaussian function. The time evolution of $f(i)$, which mirrors the one of the Overhauser field, is shown in Fig. 2(b). While the ESR frequency does not exhibit significant fluctuations in time at low field ($B = 300$ G), well-resolved spectral jumps can be observed when the magnetic field is increased. In this high magnetic field regime, the correlation time of the bath becomes longer than the measurement time T_m, which enables measuring the instantaneous Overhauser field

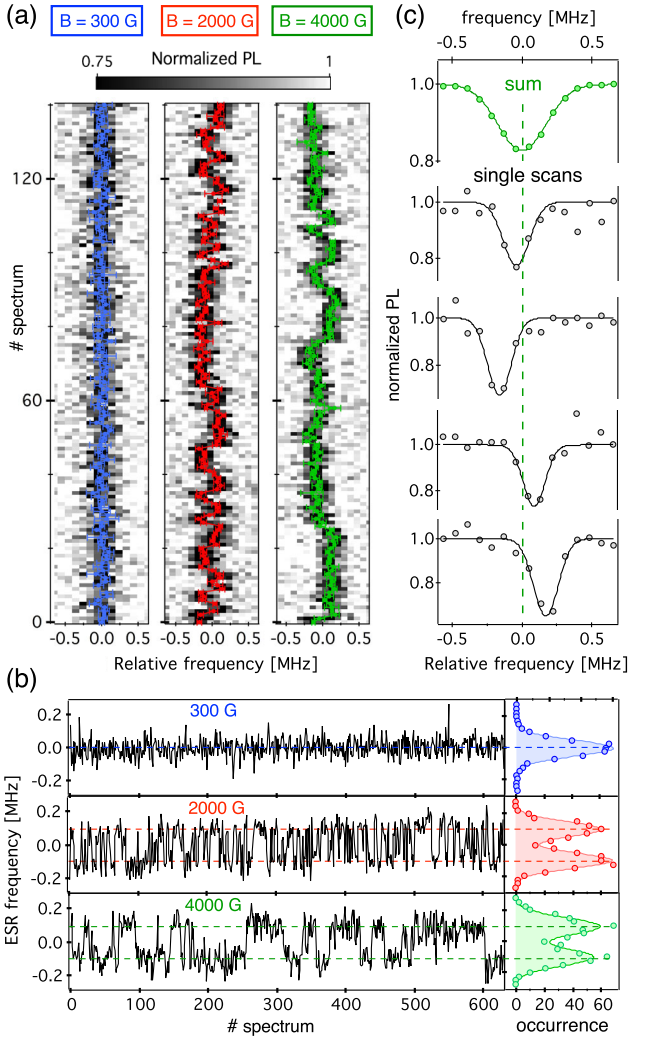

FIG. 2 (color online). (a) Intensity plots of consecutive ESR spectra recorded at different magnetic fields. Pulsed-ESR spectroscopy is performed with a MW π-pulse duration of 3 μs. Markers show the ESR frequencies obtained by fitting each individual ESR spectrum with a Gaussian function. The error bars indicate the fit uncertainty with a 95% confidence interval. (b) Time evolution of the instantaneous ESR frequency over 630 consecutive individual spectra recorded at different magnetic fields (total acquisition time ~300 s). The right panels show the corresponding histograms. (c) Top panel: Averaged sum of individual ESR spectra recorded at $B = 4000$ G. The inhomogeneous linewidth is 403 ± 6 kHz. Lower panels: Selected individual ESR spectra recorded at $B = 4000$ G. Statistical analysis over the set of 630 individual spectra leads to an ESR linewidth of 280 ± 70 kHz, limited by the π-pulse duration used for pulsed-ESR spectroscopy.

produced by different configurations of the nuclear spin bath. This is further illustrated in Fig. 2(c), where individual ESR spectra recorded at $B = 4000$ G are plotted together with the averaged sum of experimental scans (top panel). The instantaneous ESR frequencies of individual runs evolve in time and their linewidths are smaller

than the one obtained by averaging over all the configurations of the bath. As expected, spectral narrowing is also accompanied by an improved ESR contrast.

In these experiments, the amplitude of the Overhauser field fluctuations is dominated by the dynamics of the nearest ^{13}C nuclear spin of the bath, which induces a hyperfine splitting of the ESR line $\mathcal{A}^{(1)} \approx \mathcal{A}_{zz}^{(1)} \approx 200$ kHz (cf. Fig. 1) [26]. This hyperfine structure is revealed by the histograms of the instantaneous ESR frequencies $f(i)$ shown in Fig. 2(b). At low field, the histogram is well described by a normal distribution, while two peaks separated by 201 ± 3 kHz can be observed at high field. For this particular ^{13}C, the anisotropic component of the hyperfine tensor is weak, leading to a relaxation time exceeding seconds at high magnetic fields [20]. We note that the two peaks of the distribution also get broader at high magnetic field, which qualitatively indicates a contribution to the Overhauser field fluctuations from other ^{13}C nuclear spin of the reservoir (see the Supplemental Material [25]).

Measurements of the instantaneous ESR frequency can be used for narrowing down the Overhauser field distribution by postselection. For that purpose, we first consider the correlations between consecutive measurements, $f(i)$ and $f(i+1)$, whose conditional distributions are shown on Fig. 3(a) for different magnetic field amplitudes. From this set of measurements, postselection of individual ESR spectra is performed depending on the sign of the instantaneous ESR frequency. More precisely, for all measurements that satisfy $f(i) > 0$ [or $f(i) < 0$], we extract a postselected ESR spectrum by summing the set of individual runs $i+1$. The results are shown in Fig. 3(b). At low magnetic field, postselected ESR spectra are identical to the one obtained by averaging over all individual runs [black dashed line in Fig. 3(b)], pointing out the absence of correlation between consecutive measurements. At higher fields, postselected ESR spectra have a narrower linewidth (~300 kHz) with a shifted central frequency, corresponding to the hyperfine splitting of the nearest ^{13}C nuclear spin of the bath. Here, conditional measurements enable narrowing down the Overhauser field distribution by polarizing this particular ^{13}C of the bath, in the same way as in recent single shot readout experiments [20,21,27].

The linewidth of postselected ESR spectra results from the convolution of the MW excitation spectral profile and the Overhauser field distribution within the acquisition time. For a π-pulse duration of 3 μs, the width of the MW spectral profile is ~300 kHz, which is the main limitation to the ESR linewidth. Although increasing the π-pulse duration could, in principle, lead to further spectral narrowing, another consequence would be an overall reduction of the PL signal, which is limited by the duty cycle of the laser pulses in the ESR sequence. In order to keep a high signal-to-noise ratio, the measurement time per spectrum would then need to be increased, which results in averaging over a broader Overhauser field distribution.

We now analyze more quantitatively the correlations between distant individual ESR spectra by using the Allan deviation σ_A. This statistical tool is commonly used for quantifying the stability of oscillators [28] and is defined as

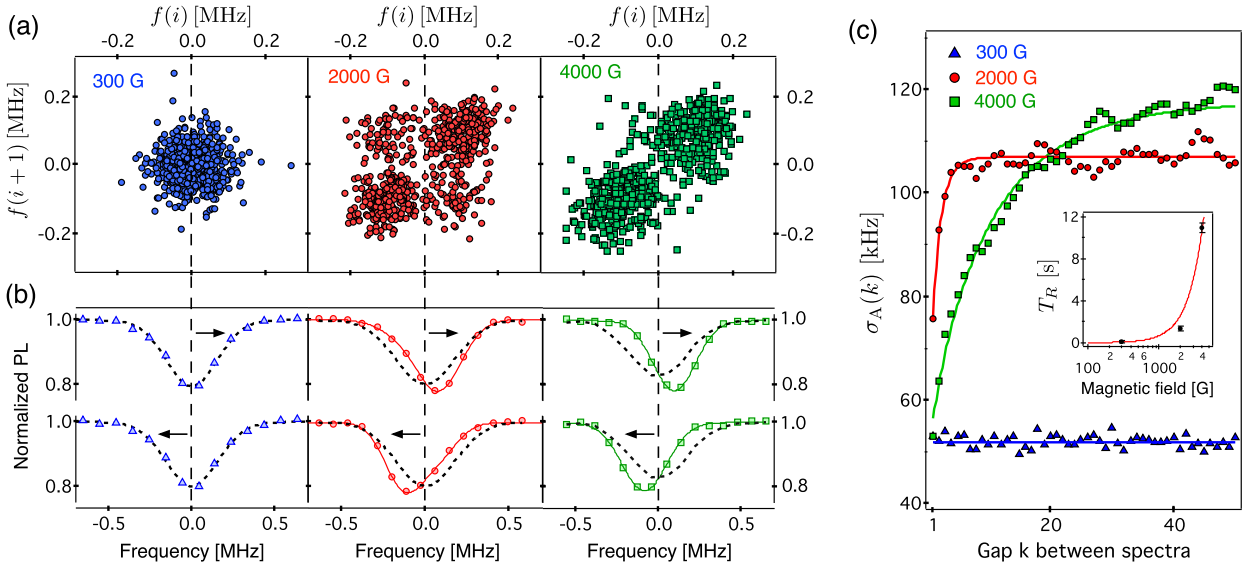

FIG. 3 (color online). (a) Distribution of consecutive ESR frequencies at three different magnetic fields. (b) Post-selected ESR spectra obtained by summing experimental runs $i+1$ conditioned by $f(i) > 0$ (upper panels) or $f(i) < 0$ (lower panels). The black dashed lines correspond to ESR spectra averaged over all individual runs. Solid lines are fits with Gaussian functions. At $B = 4000$ G, the linewidth of the postselected ESR spectrum is reduced to 303 ± 5 kHz. (c) Allan deviation $\sigma_A(k)$ inferred from the set of ESR frequencies $\{f(i)\}$ at different magnetic fields. Solid lines are data fitting with Eq. (3) leading to $\mathcal{A}^{(1)} = 210 \pm 7$ kHz. Inset: Relaxation time T_R inferred from data fitting as a function of the magnetic field. The solid line is a quadratic fit as predicted by Eq. (1).

$$\sigma_A(k) = \sqrt{\frac{1}{2}\langle [f(i) - f(i+k)]^2 \rangle_{\{i\}}}, \quad (2)$$

where $\langle \ldots \rangle_{\{i\}}$ denotes the average over all the data set $\{f(i)\}$. As shown in Fig. 3(c), the Allan deviation is flat at low field while increasing the separation k between the measurements, as expected for a regime without correlation. At high fields, the Allan deviation first increases with k before reaching a plateau. This behavior indicates strong correlations over distant individual runs. To infer quantitative information, we derive an analytical expression of the Allan deviation (see the Supplemental Material [25])

$$\sigma_A(k) = \sqrt{\sum_n \frac{\mathcal{A}_{zz}^{(n)2}}{4} [\alpha^{(n)} - \beta^{(n)2} e^{-2(k-1)T_m)/T_R^{(n)}}] + \sigma_{sn}^2}, \quad (3)$$

with

$$\alpha^{(n)} = \frac{T_R^{(n)}}{T_m}(1-\beta) \quad \text{and} \quad \beta^{(n)} = \frac{1 - e^{-2T_m/T_R^{(n)}}}{2T_m/T_R^{(n)}}.$$

Here, the sum runs over all ^{13}C nuclear spin n of the bath and σ_{sn} is the standard deviation of the measurement noise, mostly induced by shot noise (sn) in the detection of the NV center PL. This formula is simplified by considering that correlations are dominated by hyperfine interaction with the nearest ^{13}C (see the Supplemental Material [25]) and used to fit the experimental data [solid lines in Fig. 3(c)]. We obtain $\mathcal{A}_{zz}^{(1)} = 210 \pm 7$ kHz in good agreement with the value obtained by other methods [see Fig. 2(b)]. As expected, the correlation time $T_R^{(1)}$ inferred from the fit increases with the magnetic field [see inset in Fig. 3(c)], reaching more than ten seconds at 4000 G.

Every single NV defect has a specific nuclear spin environment since ^{13}C are randomly placed in the diamond lattice. The fluctuations of the Overhauser field are, therefore, expected to be different for each NV defect. To illustrate this point, the experiments were repeated with a single NV defect (denoted NV2) for which the amplitude of the Overhauser field fluctuations is not dominated by the nearest ^{13}C nuclear spin. Here, the fluctuations of the instantaneous ESR frequency can hardly be observed in consecutive ESR spectra [Fig. 4(a)]. However, the Allan deviation unambiguously indicates correlations between individual runs at high magnetic fields [Fig. 4(b)]. This observation results from the slowdown in the dynamics of some ^{13}C nuclear spins surrounding the NV defect. To check this assumption, the local ^{13}C environment was investigated by implementing a 32-pulse dynamical decoupling sequence (see the Supplemental Material [25]), which enables characterizing individual ^{13}C with hyperfine coupling strengths much smaller than the inhomogeneous ESR linewidth [29–31]. As shown in Fig. 4(c), sharp dips in the signal reveal hyperfine coupling with three individual ^{13}C nuclear spins. Table I summarizes the values of the longitudinal and anisotropic components of the hyperfine tensor extracted from the dynamical decoupling signal, following the procedure described in Ref. [29]. For this NV defect, it is very unlikely that the dynamics linked to the most strongly coupled ^{13}C will be observed, owing to the high value of its anisotropic hyperfine component. On the other hand, this component is much smaller ($\simeq$20 kHz) for the two other ^{13}C nuclear spins leading to long correlation times at high magnetic fields [see Eq. (1)]. Fitting the Allan deviation with Eq. (3) while considering

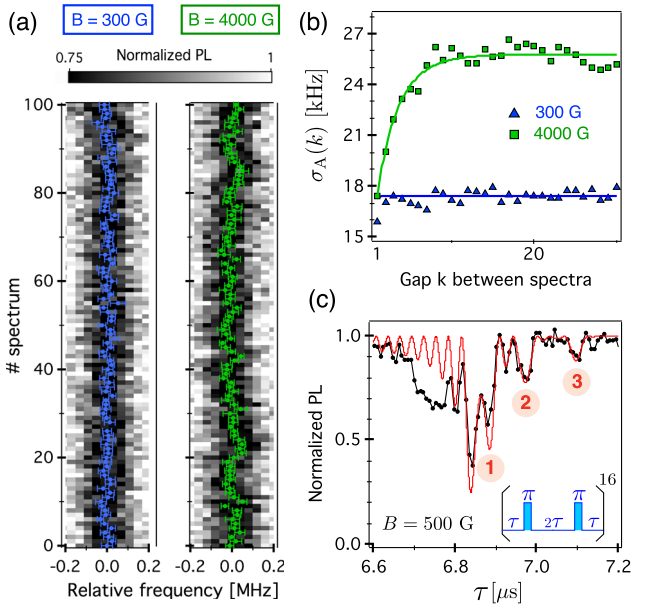

FIG. 4 (color online). (a) Intensity plots of consecutive ESR spectra recorded for NV2 with a MW π-pulse duration of 4 μs. (b) Allan deviations inferred from a set of 300 consecutive ESR spectra at different magnetic fields. Solid lines are data fitting with Eq. (3), as explained in the main text. At high fields, we obtain $T_R = 2.6 \pm 0.2$ s and $\sqrt{[\mathcal{A}_{zz}^{(2)}]^2 + [\mathcal{A}_{zz}^{(3)}]^2} = 45 \pm 2$ kHz. The latter value is in decent agreement with the one inferred from the dynamical decoupling signal (see Table I). (c) Dynamical-decoupling signal obtained by implementing a 32-pulse sequence (see inset) with a magnetic field $B = 500$ G. The solid line is data fitting using the procedure described in Ref. [29]. More details can be found in the Supplemental Material [25].

TABLE I. Longitudinal $\mathcal{A}_{zz}^{(n)}$ and anisotropic $\mathcal{A}_{ani}^{(n)}$ hyperfine components of the three ^{13}C nuclear spins detected in the dynamical decoupling signal shown in Fig. 4(c).

^{13}C number n	$\mathcal{A}_{zz}^{(n)}$ (kHz)	$\mathcal{A}_{ani}^{(n)}$ (kHz)
1	-27 ± 3	128 ± 2
2	-28 ± 2	19 ± 3
3	-46 ± 2	20 ± 3

identical relaxation time for the two ^{13}C leads to $T_R = 2.6 \pm 0.2$ s at $B = 4000$ G. These experiments demonstrate how the Allan deviation can be used to infer the relaxation time of ^{13}C with coupling strengths that are 1 order of magnitude smaller than the inhomogeneous dephasing rate of the NV defect.

In conclusion, we have used a single NV defect in diamond as a highly sensitive magnetometer to measure, in real-time, the Overhauser field produced by its nuclear spin environment under ambient conditions. Analysis of the Overhauser field fluctuations was achieved by implementing a correlation detection method based on the Allan deviation that extracts the dynamics of weakly coupled nuclear spins of the reservoir. In addition, we have reported narrowing of the Overhauser field distribution through conditional preparation of the nuclear spin bath by post-selection. Further improvements could be achieved by using stronger magnetic fields and/or by decreasing the measurement time, either by improving the collection efficiency with diamond photonic nanostructures [32,33] or by performing a single-shot readout of the NV electron spin under a cryogenic environment [34]. These methods might find applications in the context of quantum feedback control and metrology.

We thank F. Grosshans, J. P. Tetienne, and G. Hétet for fruitful discussions. This work is supported by the French National Research Agency (ANR) through the projects ADVICE and QINVC, and by the European Community's Seventh Framework Programme (FP7/2007-2013) under Grant Agreement No. 611143 (DIADEMS). J. R. M acknowledges support from Conicyt Grants Fondecyt No. 1141185, PIA Programs No. ACT1108 and No. ACT1112, and Millennium Scientific Initiative No. P10-035-F.

*Present address: Kavli Institute of Nanoscience Delft, Delft University of Technology, PO Box 5046, 2600 GA Delft, Netherlands.
a.e.dreau@tudelft.nl
†Corresponding author.
vjacques@ens-cachan.fr

[1] A. V. Khaetskii, D. Loss, and L. Glazman, Phys. Rev. Lett. **88**, 186802 (2002).
[2] A. M. Tyryshkin *et al.*, Nat. Mater. **11**, 143 (2012).
[3] G. Balasubramanian *et al.*, Nat. Mater. **8**, 383 (2009).
[4] D. Stepanenko, G. Burkard, G. Giedke, and A. Imamoglu, Phys. Rev. Lett. **96**, 136401 (2006).
[5] D. Klauser, W. A. Coish, and D. Loss, Phys. Rev. B **73**, 205302 (2006).
[6] H. Bluhm, S. Foletti, D. Mahalu, V. Umansky, and A. Yacoby, Phys. Rev. Lett. **105**, 216803 (2010).
[7] E. Togan, Y. Chu, A. Imamoglu, and M. D. Lukin, Nature (London) **478**, 497 (2011).
[8] T. D. Ladd, F. Jelezko, R. Laflamme, Y. Nakamura, C. Monroe, and J. L. OBrien, Nature (London) **464**, 45 (2010).
[9] G. Wolfowicz, A. M. Tyryshkin, R. E. George, H. Riemann, N. V. Abrosimov, P. Becker, H.-J. Pohl, M. L. W. Thewalt, S. A. Lyon, and J. J. L. Morton, Nat. Nanotechnol. **8**, 561 (2013).
[10] H. J. Mamin, M. Kim, M. H. Sherwood, C. T. Rettner, K. Ohno, D. D. Awschalom, and D. Rugar, Science **339**, 557 (2013).
[11] T. Staudacher, F. Shi, S. Pezzagna, J. Meijer, J. Du, C. A. Meriles, F. Reinhard, and J. Wrachtrup, Science **339**, 561 (2013).
[12] F. Jelezko and J. Wrachtrup, New J. Phys. **14**, 105024 (2012).
[13] N. Mizuochi *et al.*, Phys. Rev. B **80**, 041201(R) (2009).
[14] N. Zhao, S.-W. Ho, and R.-B. Liu, Phys. Rev. B **85**, 115303 (2012).
[15] J. R. Maze, A. Dréau, V. Waselowski, H. Duarte, J.-F. Roch, and V. Jacques, New J. Phys. **14**, 103041 (2012).
[16] A. Gali, M. Fyta, and E. Kaxiras, Phys. Rev. B **77**, 155206 (2008).
[17] A. Gali, Phys. Rev. B **80**, 241204 (2009).
[18] B. Smeltzer, L. Childress, and A. Gali, New J. Phys. **13**, 025021 (2011).
[19] A. Dréau, J. R. Maze, M. Lesik, J. F. Roch, and V. Jacques, Phys. Rev. B **85**, 134107 (2012).
[20] A. Dréau, P. Spinicelli, J. R. Maze, J.-F. Roch, and V. Jacques, Phys. Rev. Lett. **110**, 060502 (2013).
[21] P. C. Maurer *et al.*, Science **336**, 1283 (2012).
[22] G. Waldherr *et al.*, Nature (London) **506**, 204 (2014).
[23] A. Dréau, M. Lesik, L. Rondin, P. Spinicelli, O. Arcizet, J.-F. Roch, and V. Jacques, Phys. Rev. B **84**, 195204 (2011).
[24] P. Neumann, J. Beck, M. Steiner, F. Rempp, H. Fedder, P. R. Hemmer, J. Wrachtrup, and F. Jelezko, Science **329**, 542 (2010).
[25] See Supplemental Material at http://link.aps.org/supplemental/10.1103/PhysRevLett.113.137601 for details.
[26] The hyperfine splitting of the ESR line is expressed by $\mathcal{A}^{(n)} = \sqrt{[\mathcal{A}^{(n)}_{\mathrm{ani}}]^2 + [\mathcal{A}^{(n)}_{zz} - \gamma_n B]^2} - \gamma_n B$ [19]. In the limit of high magnetic fields, this formula simplifies as $\mathcal{A}^{(n)} = \mathcal{A}^{(n)}_{zz}$.
[27] Analysis of the data following the procedure described in Refs. [20,21] indicates a polarization efficiency exceeding 90% at $B = 4000$ G.
[28] W. J. Riley, *Handbook of Frequency Stability Analysis* (National Institute of Standards and Technology, Boulder, CO, 2008).
[29] T. H. Taminiau, J. J. T. Wagenaar, T. van der Sar, F. Jelezko, V. V. Dobrovitski, and R. Hanson, Phys. Rev. Lett. **109**, 137602 (2012).
[30] S. Kolkowitz, Q. P. Unterreithmeier, S. D. Bennett, and M. D. Lukin, Phys. Rev. Lett. **109**, 137601 (2012).
[31] N. Zhao *et al.*, Nat. Nanotechnol. **7**, 657 (2012).
[32] T. Babinec, M. Khan, Y. Zhang, J. R. Maze, P. R. Hemmer, and M. Loncar, Nat. Nanotechnol. **5**, 195 (2010).
[33] E. Neu, P. Appel, M. Ganzhorn, J. Miguel-Sánchez, M. Lesik, V. Mille, V. Jacques, A. Tallaire, J. Achard, and P. Maletinsky, Appl. Phys. Lett. **104**, 153108 (2014).
[34] L. Robledo, L. Childress, H. Bernien, B. Hensen, P. F. A. Alkemade, and R. Hanson, Nature (London) **477**, 574 (2011).